The little coadd that could: Estimating shear from coadded images

Robert Armstrong¹,^{2*}, Erin Sheldon³, Eric Huff⁴, Jim Bosch², Eli Rykoff^{5,6}, Rachel Mandelbaum⁷, Arun Kannawadi^{2,8}, Peter Melchior^{2,9}, Robert Lupton², Matthew R. Becker¹⁰, Yusra Al-Sayyed², The LSST Dark Energy Science Collaboration

- ¹Lawrence Livermore National Laboratory, Livermore, CA 94551, USA
- ²Department of Astrophysical Sciences, Princeton University, Princeton, NJ 08544, USA
- ³Brookhaven National Laboratory, Bldg. 510, Upton, NY 11973, USA
- ⁴ Jet Propulsion Laboratory, California Institute of Technology, 4800 Oak Grove Dr., Pasadena, CA 91109, USA
- ⁵ Kavli Institute for Particle Astrophysics & Cosmology, P. O. Box 2450, Stanford University, Stanford, CA 94305, USA
- ⁶SLAC National Accelerator Laboratory, Menlo Park, CA 94025, USA
- ⁷ McWilliams Center for Cosmology and Astrophysics, Department of Physics, Carnegie Mellon University, Pittsburgh, PA
- ⁸ Department of Physics, Duke University, Durham, NC 27708, USA
- ⁹ Center for Statistics and Machine Learning, Princeton University, Princeton, NJ 08544, USA 15213, USA
- ¹⁰ High Energy Physics Division, Argonne National Laboratory, Lemont, IL 60439, USA

3 July 2024

ABSTRACT

Upcoming wide field surveys will have many overlapping epochs of the same region of sky. The conventional wisdom is that in order to reduce the errors sufficiently for systematics-limited measurements, like weak lensing, we must do simultaneous fitting of all the epochs. Using current algorithms this will require a significant amount of computing time and effort. In this paper, we revisit the potential of using coadds for shear measurements. We show on a set of image simulations that the multiplicative shear bias can be constrained below the 0.1% level on coadds, which is sufficient for future lensing surveys. We see no significant differences between simultaneous fitting and coadded approaches for two independent shear codes: Metacalibration and BFD. One caveat of our approach is the assumption of a principled coadd, i.e. the PSF is mathematically well-defined for all the input images. This requires us to reject CCD images that do not fully cover the coadd region. We estimate that the number of epochs that must be rejected for a survey like LSST is on the order of $\sim 20\%$, resulting in a small loss in depth of less than ~ 0.1 magnitudes. We also put forward a cell-based coaddition scheme that meets the above requirements for unbiased weak lensing shear estimation in the context of LSST.

1 INTRODUCTION

Future large scale astronomical surveys such as the Vera C. Rubin Observatory Legacy Survey of Space and Time (LSST) (LSST Science Collaboration et al. 2009; Ivezić et al. 2019), Euclid (Laureijs et al. 2011), and the Nancy Grace Roman Space Telescope (Roman) (Spergel et al. 2015) will enable significant advances in many astronomical fields from the solar system to large scale cosmology through their unprecedented increase in the combination of depth and area coverage. The observing strategy for these surveys will repeatedly image the same patch of sky in different filters. The number of observations varies significantly between surveys and can range from only a handful to hundreds of exposures. Having repeated visits helps to build up the required depth, fill-in chip gaps, reject artifacts like cosmic rays and help achieve Nyquist sampling. Multiple observations can also help reduce systematic uncertainties, especially if they are taken on different parts of the camera and with different camera orientations.

One of the most powerful cosmological measurements from these surveys involves measuring the small distortion of galaxy images due to intervening matter. Photons from distant galaxies will be deflected by massive structures along the line of sight causing a change in the shape, brightness and position. This is known as gravitational lensing. When the changes to the galaxies are small it is referred to as "weak" lensing. Weak lensing causes the shape of nearby galaxies to be correlated as their photons pass by the same structures. Computing the correlation of the shape of galaxies at different angular separations has shown to be a powerful probe of the expansion history and growth of structure in the universe. Many past and ongoing surveys have utilized weak lensing by large-scale structure, "cosmic shear", to constrain cosmological parameters (see Giblin et al. (2021); Amon et al. (2022); Secco et al. (2022); Dalal et al. (2023); Li et al. (2023); Dark Energy Survey and Kilo-Degree Survey Collaboration et al. (2023) for recent results). However, for future surveys, one of the main challenges will be to ensure that the systematic errors are under control. There are many systematic errors that are important for weak lensing including: the choice of shear measurement algorithm, characterization of the point spread function (PSF), photometric redshifts and theoretical predictions. In this paper, we will focus on how to combine images from multiple observations of a ground-based survey, where the images are Nyquist sampled.

Weak lensing surveys have taken approaches that can be classified into three categories:

- (i) Resample all of the images to a common pixel grid and take a weighted sum to construct a single coadded image. Measurements are performed on the coadd with no need to return to the individual images.
- (ii) Perform measurements on each epoch separately. Combine these measurements at the catalog level by taking a weighted average.
- (iii) Create the coadd as in (i), but only use it to detect objects. With this information, go back to each of the individual epochs and do a joint simultaneous measurement of all the images.

The simplest option is (i), as it significantly reduces the complexity and computation time. For a survey with many epochs this is a huge gain. Many lensing surveys have chosen to work on coadded images (Hoekstra et al. 2006; Leauthaud et al. 2007; Hetterscheidt et al. 2007; Lin et al. 2012; Melchior et al. 2015; Jee et al. 2016; Dalal et al. 2023). While this approach is attractive, it can also induce a number of challenges. First, we must ensure that the individual epochs are properly registered relative to another. Mis-registered images can severely distort the shape of objects. Also, the PSF can be challenging to model on the coadd due to the discontinuous "jumps" in the shape and size of the PSF when crossing the boundary between detectors. In addition, when combining images where the size of the PSF varies widely, there will be loss in S/N by doing a simple average. We discuss these problems in more detail in Section 2. Method (ii) has been used in fewer cases (Jarvis et al. 2003). The main problem with this approach is that there will be objects that do not have a large enough S/N to be detected on any individual epoch, but will be detected on the coadd. However, there has been some work recently on how one might do this (Budavári et al. 2017).

With the need to reduce systematic errors, a number of recent surveys have followed the hybrid method (iii). The Canadian-France-Hawii Telescope Lensing Survey (CFHTLens; Heymans et al. 2013) and Kilo-Degree Survey (KiDS; Giblin et al. 2021) collaborations performed photometry and detection on the coadds and shear measurements via multi-epoch fitting. For the Dark Energy Survey (DES; Secco et al. 2022), only object detection was done on the coadd and all other measurements were performed simultaneously on individual epochs. This approach has worked well to reduce the systematic errors sufficiently low for cosmological analyses. Can this multi-epoch fitting approach be applied to future surveys as well? As the number of exposures increases, the computational demand scales as well. Existing surveys typically have fewer than ~ 10 epochs to fit simultaneously. For the Hyper-Suprime Cam Survey (HSC), a precursor to LSST, model fitting on coadds is already $\sim 40\%$ of the compute time. Extending this to work on multiple exposures will severely strain the computing budget when the number of exposures is large. Again, being able to instead work on coadded images could significantly reduce the processing burden. There may also be other reasons to prefer working on coadds. For example, when separating blended objects into their individual sources, there is limited information available on any single epoch image, making method (ii) far from optimal. The coadd is a conveniently high S/N image, reducing a potentially large bookkeeping problem with many single epoch images when using method (iii).

In this paper, we explore the possibility of avoiding multiepoch fitting by demonstrating that we can recover shear on coadds at the level required for future surveys, particularly LSST. In Section 2, we discuss the problems using coadds and and potential ways to mitigate them. Section 3 describes a set of simulations to test shear bias on both multi-epoch and coadd data. We test two separate shear measurement pipelines: Bayesian Fourier Domain (BFD) and Metacali-BRATION. We summarize how these algorithms were configured and applied in Section 4. Section 5 shows the results of these methods. We show that for both shear methods, we are able to recover the input shear signal with sufficient accuracy for both methods. Section 6 examines the loss in S/N from the coaddition itself and from rejecting exposures that would introduce a PSF discontinuity from their edges in LSST simulations. Finally, section 7 proposes a strategy to build edgefree coadds in small regions called "cells" in the context of LSST data processing.

2 COADDITION

The simplest means of combining images is to use a direct weighted mean, median or clipped mean, with each image having a single weight. The median and clipped mean are frequently used to reject artifacts in an image. None of these are optimal in measuring the flux, size or signal-to-noise ratio (S/N) because they do not properly account for variations in PSF sizes and background levels. A more important issue, however, is that not all of these methods result in the coadd image having a well-defined PSF, by which we mean that the final coadded image is the convolution of the true image with a coadd PSF at every point.

As shown in Mandelbaum et al. (2023), there are strict requirements that must be met in order for a coadd image to have a valid PSF. The first requirement is that the coaddition scheme must be linear in the pixel values. They formally demonstrate that all non-linear coaddition procedures fail to to produce a well-defined PSF. For example, in a median or clipped coadd the cores of brighter stars end up being clipped from the best seeing images, resulting in a flux-dependent (i.e., ill-defined) PSF.

Mandelbaum et al. (2023) showed that a linear coaddition scheme must also have either (a) all input images with the same PSF or (b) weights that are independent of the true signal. Using the Poisson noise of the signal in the weights will result in an ill-defined PSF. One must also be careful of using spatially-varying weights for the input images as they can introduce additional scatter in the coadd. Therefore, the simplest method to construct a coadd with a valid PSF is to use a weighted mean where the weight only depends on the background.

There are more sophisticated approaches such as Rowe et al. (2011) which constructs the coadd PSF as a linear combination of pixel values of the individual exposures in such a way to produce a well sampled coadd from undersampled input images. This will be important for space-based lensing surveys for which most images are not Nyquist-sampled. There has been renewed interest from the Roman science

team in using this approach for shear measurements (Hirata et al. 2023; Yamamoto et al. 2023)

For the majority of detections, which are small faint objects, the epochs with the smallest seeing will have the most information. Under certain assumptions, Kaiser (2004) and Zackay & Ofek (2017) constructed an optimal coadd in terms of both PSF size and information content. This results in an image that loses no information when combining epochs of different seeing. Further research in this area seems promising in order to maximize the measured S/N for a coadd. However, for this paper we only consider the scenario of using a simple weighted mean.

2.1 Image Registration and Noise

In order to coadd, we must account for the actual pointing of each image and the local distortion caused by the optics, atmosphere, etc. This requires resampling and interpolating each image onto the same coordinate grid. This interpolation procedure introduces noise correlations from one pixel to another. In addition, depending on the local distortion and relative offset between pixel grids, this can cause the noise to become non-stationary, i.e. it can vary across the image. Figure 1 shows a coadded image and variance map from the HSC UltraDeep survey (Aihara et al. 2018) where there are ~ 200 *i*-band images that were used to create the coadd. The image cutout corresponds to a region roughly $2' \times 2'$ in area. In the variance map, the darker regions have more observations and hence lower variance. The lattice-like structure corresponds to CCD edges being shifted due to the small dithering strategy employed in the UltraDeep region. The noise in this image is dominated by the changing number of input images, but smaller variations can be seen due to resampling and grid offsets. The range of variations is $\sim 10\%$ and the scale on which they vary is close to the average size of one object (see 6).

By definition, the variance map does not include the pixel to pixel covariance. This will also vary spatially depending on the dither pattern and interpolation kernel. For typical observing patterns in HSC, the amount of variance lost to covariance is $\sim 10\%$. The correlated noise pattern must be taken into account to achieve the precision in weak lensing. Gurvich & Mandelbaum (2016) showed that ignoring such correlations results in errors of a few percent, well above the requirements of future surveys. However, when such correlations are known and accounted for, their impact can be mitigated.

With a complete knowledge of the astrometric shifts and distortions, it is, in principle, possible to construct the full pixel covariance for a given region. However this is far from practical and few existing algorithms would be able to take advantage of such information. As an alternative, we follow Sheldon & Huff (2017) and take Monte Carlo realizations of the noise for each epoch and coadd them in the same way as the images. This produces a single noise image for each coadd image that includes the pixel correlations induced from interpolation. This noise image will be utilized when computing the shear in our image simulations. For our tests in this paper, we assume that the noise in each exposure is Gaussian. We found that a single noise realization per epoch was sufficient to characterize the noise.

2.2 Edge-Free Reconstruction

In many situations, we need to be able to model the PSF from the observed stars and interpolate it to the positions of galaxies. Typically, a low order polynomial is used to describe the variation of the PSF across a CCD. The challenge on a coadd is that the PSF is discontinuous across the edge of a detector from any individual epoch. Given this, it can be difficult to construct a model on the coadd. An alternative approach used by Jee et al. (2016) and Bosch et al. (2018) is to create a valid coadded PSF by resampling and interpolating the single epoch PSFs in the same way as the images. This avoids any problems of having to spatially interpolate a complex PSF model. However, objects that include an epoch which crosses a detector boundary may pose a problem, as the PSF is not well defined. For HSC DR1, objects that contained such a boundary image were flagged and corresponded to $\sim 15\%$ of the detected objects. Because the PSF is potentially inaccurate, these objects may need to be removed from scientific analyses that need an accurate PSF. Simply removing such objects will not be a viable option for a survey like LSST, as almost every object will cross at least one CCD boundary. Instead, we propose to simply throw out epochs that cross a detector boundary when creating the coadd image, PSF and noise image. The number of rejected images will depend on the size of the coadd, with fewer rejections for smaller coadds. We discuss the loss of depth from rejecting these visits in Section 6.

3 SIMULATIONS

In order test our ability to recover shear on edge-free coadds, we construct a suite of simulations to test the impact of coaddition specifically for shear estimators. The goal is to simulate multiple epochs of the same galaxy with a known shear and compare the inferred shear from both multi-epoch and coadd measurements. The observing conditions for each epoch (noise, PSF, etc.) are simulated to roughly match observations from DES data. While DES will have only ten epochs by the end of the survey, it still provides a useful test while reducing somewhat the computation time. Even with 10 epochs, the computation time to generate the dataset is significant as we need to simulate billions of galaxies to reach the needed precision for cosmic shear. With fewer epochs, we may also be more sensitive to certain systematic errors that could get averaged down for a survey with many more observations. To generate the galaxy population we use code from the nsim package which is based on GALSIM and ngmix. The generated galaxy images have the following properties:

- We generate single galaxy images on 48×48 postage stamps with no neighbors. The pixel scale is the same as DES, 0.27 arcseconds/pixel. The pixel noise is uniform for each visit and is modeled as a zero-mean Gaussian with σ chosen to be typical of DES *i*-band images.
- We assume the PSF model is perfectly known. The model is a Moffat profile (Moffat 1969) with $\beta=3.5$. The FWHM of the PSF varies for each epoch as a LogNormal distribution with mean 0.95 arcseconds and $\sigma_{\rm FWHM}=0.1$.

https://github.com/esheldon/nsim

Armstrong et al.

4

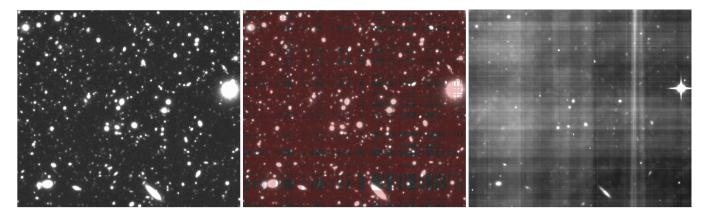


Figure 1. Left: A coadded image from the HSC UltraDeep field taken in the i-band from ~ 200 overlapping images. Middle: The same image as on the left with red lines showing the edges of CCDs. It can be seen that almost every object overlaps an edge. Right: The variance map of the image where darker colors indicate lower variance. The lattice structure is due to the small dither patterns for the HSC UltraDeep field.

Values are truncated between 0.8 and 1.15. The PSF ellipticity is Gaussian distributed with a mean of 0.0 and 0.01 for e_1 and e_2 respectively, and $\sigma_e = 0.01$. We use the same offset in PSF image as for the galaxy in its image, so that the same shifts must be applied when resampling (see §5).

- The galaxy models are pure exponentials. We sample from an empirical model for the flux and size based on COS-MOS data. We used the COSMOS I<25.2 dataset packaged along with the GALSIM software to construct a kernel density estimator for the size and flux. For the bandwidth of the estimator we use a kernel with 0.1× the intrinsic data covariance. The intrinsic ellipticity is drawn from the distribution $P(e) \propto (1-e^2)^2 \exp\left(-e^2/2\sigma_e^2\right)$ (Bernstein et al. 2016) with $\sigma_e=0.02$. In the real Universe σ_e is much larger, ~ 0.3 . The small width chosen here is set to reduce the computing time. All galaxies are sheared by $g_1=0.02$, where g is the reduced shear and g_1 is the component parallel to the x and y axes.
- We generate 10 epochs for each object. Each visit has a random shift applied in x and y that is uniform over a pixel. The Jacobian values of the WCS for each exposure are allowed to vary for each epoch. The amount of variation is taken from values measured on DES. For coaddition, we compute a mean weighted by the inverse of the pixel variance. To resample the images we use a 3rd order Lanczos kernel.
- We construct a coadded noise image, as described in Section 2.1, by generating a single Monte Carlo realization of the noise for each epoch and processing it with the same resampling used for the image, and summed with the same weights. The coadded PSF is constructed in a similar way by combining the individual PSFs for each epoch.

The choice of using simplified galaxy models was employed solely to reduce the computational run time. For more complicated models there was significant computation time in generating the images. Even with the simplifications listed, the computational cost is on the order of 10 million CPU-hours. We did some limited testing of more complicated galaxy models with reduced statistics, and these showed no sign of problems. Since both of the shear measurement pipelines employed here have already shown to be largely insensitive to the type of galaxy model chosen, we do not expect this to affect our results.

4 SHEAR MEASUREMENT METHODS

There are a number of shear measurement methods that have demonstrated the potential to meet the strict requirements for upcoming surveys. These include model fitting approaches (Miller et al. 2013), self-calibration methods (Li & Mandelbaum 2023), and Bayesian forward modeling (Schneider et al. 2015). To test our approach to measuring shear on coadds, we select the METACALIBRATION and BFD algorithms. Both of these methods have the capability to measure shear on coadd and multi-epoch data. LSST has adopted METACALIBRATIONas an official data product and the addition BFD as an additional method gives us confidence that other methods can similarly be adapted to work on coadd data. We briefly summarize the METACALIBRATION and BFD methods and describe how they were applied to these simulations.

4.1 BFD

The Bayesian Fourier Domain (BFD) method (Bernstein & Armstrong 2014; Bernstein et al. 2016) was designed to overcome some of the inherent biases that arise from the measurement of galaxy shapes. It does not measure the shapes of individual galaxies, but rather takes a probabilistic approach, estimating the probability that a galaxy would produce the pixel data for a given shear. If we assume that a set of galaxies is sheared by a constant value g, we can write the shear posterior probability by Bayes theorem as:

$$P(\boldsymbol{g}|\boldsymbol{D}) = \frac{P(\boldsymbol{D}|\boldsymbol{g})P(\boldsymbol{g})}{P(\boldsymbol{D})},\tag{1}$$

where $P(\mathbf{D}|\mathbf{g}) = \Pi_i P(D_i|\mathbf{g})$ is the probability of obtaining the pixel data D_i for the whole galaxy population. For a single galaxy we can write

$$P(D_i|\boldsymbol{g}) = \int d\boldsymbol{M}_{\text{true}} P(\boldsymbol{M}_{\text{obs}}|\boldsymbol{M}_{\text{true}}) P(\boldsymbol{M}_{\text{true}}|\boldsymbol{g}), \tag{2}$$

where we have marginalized over a set of true measurements $M_{
m true}$. If we assume that the lensing is weak, we can do a

Taylor expansion around q = 0

$$P(D_{i}|\mathbf{g}) = P_{i} + \mathbf{Q}_{i} \cdot \mathbf{g} + \frac{1}{2}\mathbf{g} \cdot \mathbf{R} \cdot \mathbf{g},$$

$$P_{i} \equiv P(D_{i}|\mathbf{g} = 0)$$

$$\mathbf{Q}_{i} \equiv \nabla_{\mathbf{g}} P(D_{i}|\mathbf{g})|_{\mathbf{g}=0}$$

$$\mathbf{R}_{i} \equiv \nabla_{\mathbf{g}} \nabla_{\mathbf{g}} P(D_{i}|\mathbf{g})|_{\mathbf{g}=0}.$$
(3)

The P_i values are the probability of measuring $M_{\rm obs}$ given the noise-free intrinsic distribution $M_{\rm true}$. We can use observations of a deeper dataset to approximate the true distribution. Most ongoing and future surveys contain a dataset suitable for this purpose. The Q_i and \mathbf{R}_i give the differential probability of observing a set of measurements under shear. If we assume that the likelihood is independent of shear, the derivatives propagate to the intrinsic distribution $P(M_{\rm true}|g)$. For the measurements we choose below and a fixed weight function, these values can be computed analytically.

We can now rewrite the shear posterior over many sources as

$$-\ln P(\boldsymbol{g}|\boldsymbol{D}) = (\text{const}) - \ln P(\boldsymbol{g}) - \sum_{i} \ln P(\boldsymbol{D}_{i}|\boldsymbol{g})$$
(4)
$$= (\text{const}) - \ln P(\boldsymbol{g}) - \boldsymbol{g} \cdot \boldsymbol{Q}_{\text{tot}} + \frac{1}{2} \boldsymbol{g} \cdot \mathbf{R}_{\text{tot}} \cdot \boldsymbol{g},$$

$$\boldsymbol{Q}_{\text{tot}} \equiv \sum_{i} \frac{\boldsymbol{Q}_{i}}{P_{i}}$$
(5)

$$\mathbf{R}_{\text{tot}} \equiv \sum_{i} \left(\frac{\mathbf{Q}_{i} \mathbf{Q}_{i}^{T}}{P_{i}^{2}} - \frac{\mathbf{R}_{i}}{P_{i}} \right) \tag{6}$$

If we ignore the prior, we can write the shear posterior distribution as a Gaussian in q, with mean value

$$\bar{\mathbf{g}} = \mathbf{R}_{\text{tot}}^{-1} \mathbf{Q}_{\text{tot}}.\tag{7}$$

We can account for selection effects by adding an additional term to both $Q_{\rm tot}$ and $\mathbf{R}_{\rm tot}$ that computes the probability we would select an object given a set of cuts on our measurements. It is important that the selection criteria only depend on our set of measurements $M_{\rm obs}$. We use the postage stamp correction scheme as described in Section 2.3 of Bernstein et al. (2016).

For our measurements we compress the pixel data into a set of moments, M_{obs} in Fourier space

$$\boldsymbol{M}_{\text{obs}} \equiv \begin{pmatrix} M_f \\ M_r \\ M_+ \\ M_{\times} \end{pmatrix} = \int d^2k \, \frac{\tilde{I}^o}{\tilde{T}(\boldsymbol{k})} W(|\boldsymbol{k}^2|) \begin{pmatrix} 1 \\ k_x^2 + k_y^2 \\ k_x^2 - k_y^2 \\ 2k_x k_y \end{pmatrix},$$
(8)

where \tilde{I}^o is the Fourier transform of the image and $\tilde{T}(\boldsymbol{k})$ is the Fourier transform of the PSF and $W(|\boldsymbol{k}^2|)$ is a fixed weight function to bound the noise.

As noted in Bernstein et al. (2016), because the BFD moments are linear, measurements on multiple exposures can be combined at the catalog level by taking weighted sums of the individual moments. This is true as long as each individual exposure is unaliased. This greatly simplifies doing a multi-exposure measurement compared to other methods because there is no need to go back to the individual pixels. For measurements on the coadd, we need to have an accurate

measure of the pixel noise power spectrum. We can measure this directly from the resampled and coadded noise images.

We configure the BFD code to run with the following parameters:

• We use the ' $k\sigma$ ' weight function defined in Bernstein et al. (2016):

$$W(|k^2|) \equiv \begin{cases} \left(1 - \frac{k^2 \sigma_k^2}{2N}\right)^N & k < \frac{\sqrt{2N}}{\sigma_k} \\ 0 & k \geqslant \frac{\sqrt{2N}}{\sigma_k} \end{cases}$$
(9)

The parameters are set to N=4 and $\sigma_k=1$. We chose σ_k to be smaller than in Bernstein et al. (2016). This removes the small shear bias observed in the image simulations from that study. Other parameters were chosen to match those listed in the GALSIM settings from Table 1 in Bernstein et al. (2016).

- We simulated a deep dataset with the same settings, except the pixel noise was reduced by a factor of 100.
- We divide the data into two different regimes: flux signal-to-noise (S/N) between 5-25 and between 25-50. We build a separate prior for each regime. For the higher S/N range, we doubled measured moment noise to increase the overlap with the relatively small number of deep galaxies. This is to account for the fact that higher S/N galaxies will have a smaller measurement error and narrower likelihood, and will therefore overlap fewer templates. See Bernstein et al. (2016) Section 2.5 for more details.

4.2 Metacalibration

METACALIBRATION is a method to calibrate weak lensing shear measurements using transformations of the real images, without reference to external data sets or simulations (Huff & Mandelbaum 2017; Sheldon & Huff 2017). Below we give a brief review of the METACALIBRATION formalism. For full details of the METACALIBRATION implementation used in this work, see Sheldon & Huff (2017).

The basic assumption behind METACALIBRATION is that the two-component shear estimator e is linearly related to the applied shear g, such that

$$e = e|_{g=0} + \frac{\partial e}{\partial g}\Big|_{g=0} g + \dots$$

$$\equiv e|_{g=0} + Rg + \dots$$
(10)

We have defined the 2×2 shear response matrix

$$\mathbf{R} \equiv \frac{\partial \mathbf{e}}{\partial \mathbf{g}} \bigg|_{q=0}.\tag{11}$$

With METACALIBRATION these derivatives are performed by shearing the real image of the object and calculating a finite difference derivative. The image is deconvolved with the PSF, sheared by a small amount, and reconvolved by a larger PSF to suppress amplified noise. Measurements e are then made on these images and the derivatives are formed. For element i, j

$$R_{i,j} = \frac{e_i^+ - e_i^-}{\Delta q_i},\tag{12}$$

where e^+ is the measurement made on an image sheared by +g, e^- is the measurement made on an image sheared by -g, and $\Delta g = 2g$. For the measurement of simple mean shear,

which is all we will use in this work, the calibrated estimator is formed using the ensemble mean of the estimator and response

$$\langle e \rangle = \langle e \rangle|_{g=0} + \langle Rg \rangle + \dots$$

 $\approx \langle Rg \rangle,$ (13)

and thus

$$\langle \hat{\gamma} \rangle = \langle \mathbf{R} \rangle^{-1} \langle \mathbf{e} \rangle \approx \langle \mathbf{R} \rangle^{-1} \langle \mathbf{R} \mathbf{g} \rangle. \tag{14}$$

Note that if selections are performed on the measurements, an additional response R_S must be calculated and added to the ensemble response to correct for shear-dependent selection effects (Sheldon & Huff 2017).

The convolutions and shears applied to the images result in correlated noise that can bias the shear estimate. We apply a simple empirical correction. We generate a noise image with the same amplitude as the noise in the real data, and the same shape as original image. We rotate the noise image by 90 degrees. We apply METACALIBRATION shearing and convolution operations. We then rotate this field back by 90 degrees and add it to the image of the object before performing a measurement. This cancels the correlated noise bias in the ensemble shear measurement (Sheldon & Huff 2017).

Resampling involves interpolation of the images, which introduces additional correlated noise. This can be dealt with in the same correlated noise correction scheme. We generate noise images as described above, but pass them through resampling and summing before passing them through the METACALIBRATION convolution and shearing operations.

5 SIMULATION RESULTS

We ran the BFD and METACALIBRATION shear measurement codes on our simulations in both multi-epoch mode and on the coadded images. Each method was used on independent data sets so the resulting errors are uncorrelated. For METACALIBRATION we made consistent cuts on coadd and multi-epoch objects such that S/N>10 and square size relative to the PSF of $T/T_{\rm PSF}>0.5$. We used the size defined as $T=\langle x^2+y^2\rangle$ from the second moments of the brightness profile. For BFD we made cuts on the flux of 5<S/N<50 as described in 4.1. We applied corrections for selection effects in both methods which are needed to get the required precision.

We tested the accuracy of our methods by comparing the measured value of g_1 to the input of the simulations. One common metric is to compute the multiplicative bias m and additive bias c defined by

$$g_{\text{meas}} - g_{\text{true}} = mg_{\text{true}} + c. \tag{15}$$

We found that c was consistent with zero for all the tests we ran and therefore show only the results for m. In Table 1 we summarize the measured bias on g_1 for each shear method and for coadd vs. multi-epoch fitting. For g_2 , we found the measured values consistent with zero as expected. These results show that there is no additional bias in either shear method when measuring the shear on the coadds. Ambitious future surveys require the shear bias to be $< 10^{-3}$ (Huterer et al. 2006; Amara & Réfrégier 2008) in order to keep the bias from degrading the accuracy of cosmological analyses. This number is for all weak lensing systematics that could

Sample	Multiplicative bias for g_1
BFD Coadd BFD Multi-epoch METACALIBRATION Coadd METACALIBRATION Multi-epoch	$\begin{array}{c} 0.0012 \pm 0.0007 \\ -0.0014 \pm 0.0007 \\ 0.0007 \pm 0.0004 \\ 0.0004 \pm 0.0004 \end{array}$

Table 1. The measured shear bias from simulations for BFD and METACALIBRATION on both coadd and multi-epoch data. These results show no statistically significant bias for any of the methods beyond that expected from the breakdown of the weak shear approximation (~ 0.0005). Measured errors on the bias are 1σ .

contribute to a bias in the shear. Both methods demonstrate that coaddition does not contribute the bias for these simulations

We note additional findings from our analysis:

- The Monte Carlo noise images that we generated for each epoch were the same size as the galaxy postage stamp; 48 by 48 pixels. If the size of the noise image is reduced we see a bias in the BFD results. Reducing the noise image to 40 by 40 results in a $\sim 1\%$ bias and increases with decreasing size. Presumably, this comes from not having sufficient information to construct the power spectrum accurately on the final coadd. Note that METACALIBRATION has a strict requirement that the noise image must be at least as large as the original image.
- We placed the PSF from each image at the same subpixel offset as the galaxy so that a shift was required during resampling. This is required so that the same small smoothing due to interpolation is present in both the image and PSF image. BFD did not seem sensitive to the centering of the PSF, while METACALIBRATION required a high order interpolation kernel if the PSF was properly off center before resampling. BFD was likely less sensitive to this because the same centering error was in the deep reference set and the shallower images, so this problem was being calibrated out.
- We tested coadds created from the original simulation images that had large random rotations as LSST will for camera rotations. We found no additional bias, as long as the images were padded sufficiently to avoid corner effects.
- A detailed study testing the accuracy of cell-based coadds (see Section 7) on LSST-like simulations has also been done for an extension of METACALIBRATION called METADETECTION (Sheldon et al. 2023). This study did more realistic simulations than this work including things like realistic galaxy models, galaxy blends, stars, and cosmic rays. They showed that METADETECTION measured no shear bias to within the requirements of LSST.

6 S/N LOSS IN EDGE-FREE COADDS

For edge-free coadds it is important to understand how much information will be lost. This lost information will come from the coaddition process itself and also due to the rejection of edge exposures, images that do not fully cover the coadd. While, some of this lost information could be recovered using optimal methods for coaddition, we again restrict our analysis to using a weighted mean for coaddition.

6.1 Expected Flux S/N Loss from Coaddition

For the simple weighted mean coadds used in this work, we expect measurements on a coadd to be noisier than those using optimal multi-epoch fitting when the size of the PSF varies between epochs. We expect the increase in noise to be largest for the smallest objects such as stars and distant galaxies, the images of which are more affected by the PSF.

To gain some intuition, we derive the functional form of the expected loss in S/N for the case of a linear fit for the amplitude A of a template, or "matched filter". In this case we can analytically compute the uncertainty in the estimated flux, \hat{A} , from a linear fit to the data (see Appendix A). It is also useful to introduce a "toy model", which illustrates the main features of this process. For the toy model we use data that follows a circular Gaussian, which makes the calculations easier and allows introduction of useful approximations.

In Appendix A we derive the full expression for the variance in the multi epoch and coadd cases. We also show that (see equation A17), for the toy model and small variations in the PSF size, the ratio of the flux variance derived from the coadd to that from fitting the epochs simultaneously is approximately:

$$\left(\frac{\operatorname{var}\hat{A}_{\operatorname{coadd}}}{\operatorname{var}\hat{A}_{\operatorname{multi}}}\right)_{\operatorname{toy}} \approx 1 + 2\left(1 - R\right)^2 \left(\frac{\Delta\sigma_p}{\sigma_p}\right)^2,$$
 (16)

where σ_p is the mean PSF size, $\Delta \sigma_p$ is the RMS scatter in PSF size across the individual visits, and $R = \sigma_g^2/(\sigma_p^2 + \sigma_g^2)$ is the ratio of the pre-seeing galaxy size σ_g^2 to the post-seeing galaxy size $\sigma_p^2 + \sigma_g^2$. This result shows the increased variance is proportional to $(1-R)^2$ and the relative variation in PSF size $(\Delta \sigma_p/\sigma_p)^2$. For a large galaxy R is near unity and for a star R is near zero, so as expected the effect is largest for stars.

We tested the validity of equation (16) using a simple Monte Carlo simulation. We used the GALSIM package (Rowe et al. 2015) to generate images of circular Gaussian galaxies, convolved by circular Gaussian PSFs, and used the ngmix package² to fit for the flux. We used a PSF with FWHM=0.9 arcseconds and pixel scale of 0.26, with Gaussian variation between images of $\Delta \sigma_p/\sigma_p=0.1$.

All objects were placed at the center of the image, so that no interpolation was required when coadding the images. We used the same constant noise for all images, and used a simple mean for the coaddition process. The primary variable of interest is the resolution R. We varied the size of the galaxy from zero, or star-like, to more than twice the PSF size, such that $\langle R \rangle = 0.83$. A comparison of the results from the simulations and analytical formula are shown in Figure 2. The points are the measured values and the solid line is the ratio of the exact variance estimate from (A5) and (A7). The dotted lines are the predicted values from the toy model in equation (16). As expected the exact estimators describe the results well. The toy model slightly over-predicts the increase in variance, but is evidently useful for understanding how the effect scales with resolution. For a given survey we can use this to predict the effect that coaddition will have on the flux uncertainty.



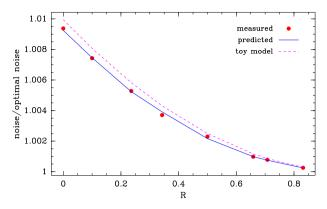


Figure 2. The ratio of the noise in the estimated flux when measured on a coadd compared to an optimal combination of images when both the galaxy and PSF are Gaussian. The horizontal axis is a dimensionless measure of the galaxy size compared to the total PSF-convolved object size, $R = \sigma_g^2/(\sigma_p^2 + \sigma_g^2)$, where σ_g is the galaxy size and σ_p is the PSF size. The points are measured values from simulations, and the solid line is the ratio of equations (A5) and (A7). The dashed line shows the simple toy model presented in equation (16).

While the numbers used to generate Fig. 2 match the values we used in our simulations from Section 3, surveys like LSST will have a wider range of seeing values and therefore larger $\Delta \sigma_n / \sigma_n$. To estimate this value for LSST, we use data generated by the "Operations Simulator" (OPSIM) (Delgado & Reuter 2016; Reuter et al. 2016). OPSIM includes an estimated seeing for all exposures over a full 10-year simulated LSST survey. Using a recent baseline observing schedule (version 3.2³(Jones et al. 2020)), we compute $\Delta \sigma_p/\sigma_p \approx 0.3$ and $\sigma_p \approx 0.4$ arcseconds. For these values, the ratio of the coadd noise relative to the optimal noise increases to ~ 1.2 for stars (R=0) and to ~ 1.01 for the largest galaxies (R=0.8). For typical galaxies used in weak lensing, this will not be a large effect, but may be a noticeable source of noise for smaller objects. One approach to reduce the added noise would be to generate multiple coadds in different bins of seeing. This approach would reduce the number of simultaneous images to analyze and limit the range of seeing values. We leave investigation of the optimal way to build LSST coadds for weak lensing to future work.

6.2 S/N Loss from Rejecting Exposures

We can estimate how many exposures would be rejected for different cell sizes using the previously mentioned OPSIM data. It includes information on where the camera is pointing at any given time during the survey. We use a slightly older OPSIM strategy labeled as minion_1016 used by the Dark Energy Science Collaboration to generate the Data Challenge 2 data (LSST Dark Energy Science Collaboration (LSST DESC) et al. 2021).

By default the simulation does not provide a dithering strategy for different exposures of the same pointing, therefore we we implemented a number of different dither strate-

³ https://s3df.slac.stanford.edu/data/rubin/sim-data/ sims_featureScheduler_runs3.2/baseline/baseline_v3.2_ 10yrs.db

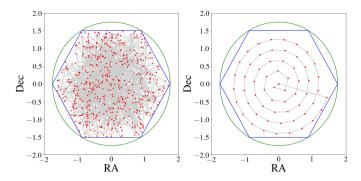


Figure 3. Two different LSST dither patterns are shown taken from LSST Science Collaboration et al. (2017). On the left each visit gets a random position and on the right a spiral pattern. Each dot shows a separate offset from the nominal pointing. The green circle represents the approximate size of the LSST focal plane. The dots are restricted to within the blue hexagon for this study.

gies as provided by the LSST Metrics Analysis Framework (MAF) software (LSST Science Collaboration et al. 2017). We found that the results had little dependence on which dithering strategy was chosen, therefore we will only show two representative dither patterns - a random offset for each visit and a spiral pattern. Fig. 3 shows the distribution of offsets for these two patterns.

We compute the number of missing exposures by placing 10,000 square patches of a given size on the sky and calculating the number of r-band visits that have a CCD edge that will cross each patch. From this, we can calculate the reduced r-band 5σ point source depth for each patch that would result from rejecting these exposures. Fig. 4 shows the 5σ cell depth for three different cell sizes with side length 0.1, 0.5 and 0.8 arcminutes. Given these cell sizes, the fraction of rejected visits can vary from 3% to 20%. (The variation in depth can also affect the science results, see Heydenreich et al. (2020))

To connect the cell sizes with observations, we need to know the typical object size in LSST. Because we want to avoid splitting blended galaxies, we use the combined size of all galaxies identified as coming from the same blend. We can estimate these sizes from the HSC UltraDeep (Aihara et al. 2018) Data Release 1 which has a depth of ~ 27.5 , comparable to the wide field LSST depth. As a proxy for size, we use the square root of the area of the bounding box for all blended objects detected in the HSC data. Fig. 5 shows the cumulative distribution along with vertical lines for our chosen patch sizes. It indicates that $\sim 80\%$ of objects would fit in a patch size of 0.1 arcminutes and we reach $\sim 99\%$ at a size of 0.36 arcminutes. We therefore conclude that a cell size near 1 arcminute will fully contain almost all objects.

7 BUILDING CELL-BASED COADDS FOR LSST

Another challenge for edge-free coadds is how to choose a region of interest to coadd. For our simulations above, we used a per-object coadd. This presents challenges for real data that needs to deal with the complications of object identification and galaxy blending (Melchior et al. 2021). A more practical approach is to build coadds in small regions on the

sky called "cells". Larger cells reject more exposures, but are less sensitive to the details of how galaxies are defined.

To implement cell-based coadds for LSST data processing, we must add an additional layer of complexity to account for cells. Our approach for building cells is based on a strategy devised for the Dark Energy Survey (Becker & DES Collaboration 2024) and adapted to the LSST pipeline. The full sky is divided into a set of square "tracts" that share the same tangent plane projection. Each tract contains a grid of square "patches" that are typically tens of arcminutes on a side and have some amount of overlap. Given that we want the size of our cells to be at arcminute scales, we need to further subdivide each patch into overlapping cells. To meet this requirement, the patches are defined as integral multiples of cells, and tracts are defined as integral multiples of patches. Fig. 6 shows a visual example of a single patch divided into multiple cells. While the exact sizes are yet to be determined, a tract is typically on the order of 1-2 degrees on each side.

The inner region of the cells tile the sky. To account for objects that may extend beyond the inner regions of a given cell, an extra boundary area is included in each cell that will overlap with neighboring cells. This buffer area can reduce problems that come from edge effects within a cell. To remove duplicate objects from these regions, catalogs must be trimmed to the unique area of each cell. This buffer area increases the amount of storage needed for cell-based coadds by a factor of a few over the standard patch-based storage.

An implementation of cell-based coadd data structure is currently being incorporated into the LSST software⁴ and will likely be the default images on which shear will be measured. This data structure can hold multiple realistic noise realizations that will be required for shear estimation algorithms. Cell-based coadds may also have additional benefits over the standard patch-based coadds. For example, because cell-based coadds are small, the PSF on the coadd will have little spatial variation. Therefore, it may be sufficient to use the PSF at the center of the cell. This would make the PSF fast to compute compared to patch-based coadds which requires warping the PSF from individual exposures and coadding them on the fly for each evaluation of the PSF. For data with many epochs, this operation dominates the compute time and makes it difficult to process patches in a reasonable amount of time. We leave the details of how to best construct cell-based coadds for LSST to future work

8 SUMMARY

We have shown that weak lensing shear can be reliably inferred using coadded images that have a well-defined PSF. We tested two state-of-the art shear techniques, BFD and METACALIBRATION, and in both cases we detected no additional bias due to coaddition. We see minimal loss of information using non-optimal weighted mean coadds for the case of relatively small PSF size variations (of order ten percent). The two shear inference methods have quite different assumptions, lending support to the notion that the use of coadds may be possible for other methods as well. We expect that other shear measurement methods would also be able work on coadds as long as they can correctly account for the correlated noise that arises during the coaddition process. We have explicitly assumed in this study that the coadded noise

⁴ https://github.com/lsst/cell_coadds

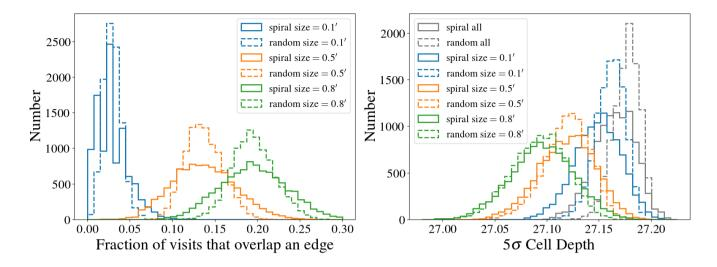


Figure 4. Left: The fraction of visits that would need to be rejected from a patch for three different patch sizes (0.1, 0.5 and 0.8 arcminutes) and the two dither patterns shown in Fig. 3. Right: The corresponding distribution of 5σ depths for each patch.

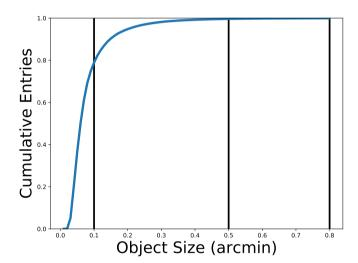


Figure 5. The cumulative distribution of blended galaxy sizes from the HSC UltraDeep data with vertical lines indicating the cell sizes we chose.

field is roughly constant over the size of an object. The scale of noise variation will depend on the distortion, warping, etc. which could potentially change for different surveys.

These tests were done on simple inverse variance weighted coadds which are relatively easy to construct. However, there are some cases where this approach may not be optimal. For example, using such simple coadds will likely somewhat degrade the ability to classify stars and galaxies, as the width of the coadded PSF is necessarily larger than that of the best input images. In this case there is a clear benefit to constructing optimal coadds. Exploring this in more detail is beyond the scope of this work.

We did not address science cases beyond weak lensing shear inference and simple flux measurements. Other science cases may have different needs. For example, it is likely that some

form of multi-epoch fitting will be needed for effective detection and characterization of moving objects.

The cost of applying our approach to real data is that epochs which cross CCD boundaries must be rejected from the coadd, in order to preserve the continuity of the PSF. We describe a potential strategy for LSST that builds cell-based coadds where the size of a cell is a few arcminutes on a side. Shear measurements, and potentially others, would be performed on these cells. Using a combination of existing data and simulations, we showed that for cells of ~ 1 arcminute on a side most objects would fit inside this cell and that the resulting number of exposures we would reject on average would be somewhere between 10-20%. This would lead to a small loss in depth (~ 0.1 mag), but would dramatically increase the processing speed while reducing complexity compared to multi-epoch fitting, without a loss in accuracy.

This work is especially relevant for surveys with many exposures like LSST. Multi-epoch fitting will dominate the compute resources for such a survey and therefore anything that can alleviate that will be extremely helpful. We have shown that the computational cost for shear estimation can be significantly reduced by using using coadded images instead of the more optimal multi-epoch fitting approach.

The weak lensing literature includes studies that take a wide variety of approaches to shear inference in multi-epoch data. In this work, we have sought to place the choice of approach on a firmer foundation (at least for Nyquist sampled ground-based images) by exploring issues of shear bias, statistical uncertainty, and the handling of objects near the boundaries of detectors in detail. While some implementation details were deferred to future work, our results suggest that current and future ground-based weak lensing studies that adopt a principled coaddition method of the sort described in this work may be well-justified in the use of coadds for shear inference.

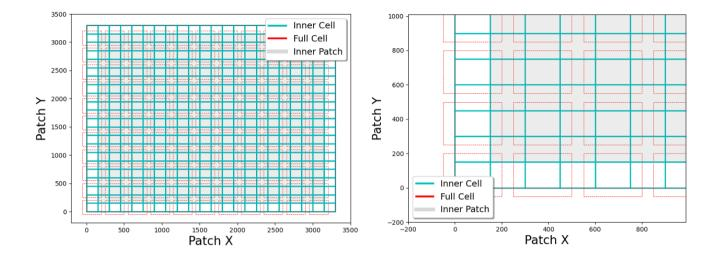


Figure 6. An example layout of cell-based coadds. *Left*: A full patch is displayed with the inner boundary of each cell outlined cyan. The full cell is outlined in red, but is only drawn for every other cell to reduce the number of lines on the plot. The grey region indicates the inner boundary of the patch. *Right*: A zoomed in view of the patch near the lower left-hand corner, where again only every other full cell is plotted to reduce the number of lines.

ACKNOWLEDGMENTS

This paper has undergone joint internal review in the LSST Data Management team and the LSST Dark Energy Science Collaboration. The primary authors would like to thank the internal reviewers Joshua Meyers, Arun Kannawadi, and Andrés Plazas Malagón for their comments.

Author contributions are as follows: R. Armstrong performed the shear tests of the BFD method, ran the OPSIM simulations and was the primary author of the paper. E. Sheldon performed tests of the METACALIBRATION method, contributed to testing and deriving the analytic S/N loss function, and provided feedback on the document. E. Huff contributed to deriving the analytic S/N loss function. Eli Rykoff wrote the cell-based patch-building code for LSST data management. J. Bosch provided many useful suggestions and discussions and feedback on the paper. R. Mandelbaum gave many useful suggestions and provided feedback on various drafts of the paper. A. Kannawadi contributed text on cellbased coadds for LSST and gave many helpful comments as a reviewer. M. Becker contributed the ideas on how to embed cell-coadds into the Rubin tract/patch coordinate system. P. Melchior was involved in many early discussions and gave feedback on the paper. R. Lupton helped to shape the scope of the project through many early discussions. Y. Al-Sayyed participated in discussions on implementing cell-based coadds into the LSST software.

This material is based upon work supported in part by the National Science Foundation through Cooperative Agreement 1258333 managed by the Association of Universities for Research in Astronomy (AURA), and the Department of Energy under Contract No. DE-AC02-76SF00515 with the SLAC National Accelerator Laboratory. Additional LSST funding comes from private donations, grants to universities, and in-kind support from LSSTC Institutional Members. RM is supported by the US Department of Energy Cosmic Frontier program, grant DE-SC0010118.

The DESC acknowledges ongoing support from the Institut National de Physique Nucléaire et de Physique des Particules in France; the Science & Technology Facilities Council in the United Kingdom; and the Department of Energy, the National Science Foundation, and the LSST Corporation in the United States. DESC uses resources of the IN2P3 Computing Center (CC-IN2P3-Lyon/Villeurbanne - France) funded by the Centre National de la Recherche Scientifique; the National Energy Research Scientific Computing Center, a DOE Office of Science User Facility supported by the Office of Science of the U.S. Department of Energy under Contract No. DE-AC02-05CH11231; STFC DiRAC HPC Facilities, funded by UK BEIS National E-infrastructure capital grants; and the UK particle physics grid, supported by the GridPP Collaboration. This work was performed in part under DOE Contract DE-AC02-76SF00515.

This work was performed under the auspices of the U.S. Department of Energy (DOE) by Lawrence Livermore National Laboratory (LLNL) under Contract DE-AC52-07NA27344, with IM release number LLNL-JRNL-866228. Funding for this work was provided as part of the DOE Office of Science, High Energy Physics cosmic frontier program. This document was prepared as an account of work sponsored by an agency of the United States government. Neither he United States government nor Lawrence Livermore National Security, LLC, nor any of their employees makes any warranty, expressed or implied, or assumes any legal liability or responsibility for the accuracy, completeness, or usefulness of any information, apparatus, product, or process disclosed, or represents that its use would not infringe privately owned rights. Reference herein to any specific commercial product, process, or service by trade name, trademark, manufacturer, or otherwise does not necessarily constitute or imply its endorsement, recommendation, or favoring by the United States government or Lawrence Livermore National Security, LLC. The views and opinions of authors expressed herein do not necessarily state or reflect those of the United States government or Lawrence

Livermore National Security, LLC, and shall not be used for advertising or product endorsement purposes.

DATA AVAILABILITY

While the simulated data we used for this analysis was not saved, the code used to generate the underlying data will be shared on reasonable request.

REFERENCES

```
Aihara H., et al., 2018, PASJ, 70, S8
Amara A., Réfrégier A., 2008, MNRAS, 391, 228
Amon A., et al., 2022, Phys. Rev. D, 105, 023514
Becker M., DES Collaboration 2024
Bernstein G. M., Armstrong R., 2014, MNRAS, 438, 1880
Bernstein G. M., Armstrong R., Krawiec C., March M. C., 2016,
   MNRAS, 459, 4467
Bosch J., et al., 2018, PASJ, 70, S5
Budavári T., Szalay A. S., Loredo T. J., 2017, ApJ, 838, 52
Dalal R., et al., 2023, arXiv e-prints, p. arXiv:2304.00701
Dark Energy Survey and Kilo-Degree Survey Collaboration et al.,
   2023, The Open Journal of Astrophysics, 6, 36
Delgado F., Reuter M. A., 2016, in Observatory Opera-
   tions: Strategies, Processes, and Systems VI. p. 991013,
   doi:10.1117/12.2233630
Giblin B., et al., 2021, A&A, 645, A105
Gurvich A., Mandelbaum R., 2016, MNRAS, 457, 3522
Hetterscheidt M., Simon P., Schirmer M., Hildebrandt H., Schrab-
   back T., Erben T., Schneider P., 2007, A&A, 468, 859
Heydenreich S., et al., 2020, A&A, 634, A104
Heymans C., et al., 2013, MNRAS, 432, 2433
Hirata C. M., et al., 2023, arXiv e-prints, p. arXiv:2303.08749
Hoekstra H., et al., 2006, ApJ, 647, 116
Huff E., Mandelbaum R., 2017, preprint, (arXiv:1702.02600)
Huterer D., Takada M., Bernstein G., Jain B., 2006, MNRAS, 366,
Ivezić Ž., et al., 2019, ApJ, 873, 111
Jarvis M., Bernstein G. M., Fischer P., Smith D., Jain B., Tyson
   J. A., Wittman D., 2003, AJ, 125, 1014
Jee M. J., Tyson J. A., Hilbert S., Schneider M. D., Schmidt S.,
   Wittman D., 2016, ApJ, 824, 77
Jones R. L., Yoachim P., Ivezic Z., Neilsen E. H., Ribeiro
   T., 2020, Survey Strategy and Cadence Choices for the
   Vera C. Rubin Observatory Legacy Survey of Space and
   Time (LSST), doi:10.5281/zenodo.4048838, https://doi.org/
   10.5281/zenodo.4048838
Kaiser N., 2004, Internal Pan-STARRS Document
LSST Dark Energy Science Collaboration (LSST DESC) et al.,
   2021, ApJS, 253, 31
LSST
        Science
                  Collaboration
                                              2009,
                                                      preprint,
   (arXiv:0912.0201)
LSST
        Science
                  Collaboration
                                        al..
                                              2017.
                                                      preprint,
   (arXiv:1708.04058)
Laureijs R., et al., 2011, preprint, (arXiv:1110.3193)
Leauthaud A., et al., 2007, ApJS, 172, 219
Li X., Mandelbaum R., 2023, MNRAS, 521, 4904
Li X., et al., 2023, Phys. Rev. D, 108, 123518
Lin H., et al., 2012, ApJ, 761, 15
Mandelbaum R., Jarvis M., Lupton R. H., Bosch J., Kannawadi
   A., Murphy M. D., Zhang T., LSST Dark Energy Science Col-
   laboration 2023, The Open Journal of Astrophysics, 6, 5
```

Melchior P., et al., 2015, MNRAS, 449, 2219

Nature Reviews Physics, 3, 712

Melchior P., Joseph R., Sanchez J., MacCrann N., Gruen D., 2021,

```
Miller L., et al., 2013, MNRAS, 429, 2858
Moffat A. F. J., 1969, A&A, 3, 455
Reuter M. A., Cook K. H., Delgado F., Petry C. E., Ridgway S. T.,
   2016, in Modeling, Systems Engineering, and Project Manage-
   ment for Astronomy VI. p. 991125, doi:10.1117/12.2232680
Rowe B., Hirata C., Rhodes J., 2011, ApJ, 741, 46
Rowe B. T. P., et al., 2015, Astronomy and Computing, 10, 121
Schneider M. D., Hogg D. W., Marshall P. J., Dawson W. A.,
   Meyers J., Bard D. J., Lang D., 2015, ApJ, 807, 87
Secco L. F., et al., 2022, Phys. Rev. D, 105, 023515
Sheldon E. S., Huff E. M., 2017, ApJ, 841, 24
Sheldon E. S., Becker M. R., Jarvis M., Armstrong R., LSST Dark
   Energy Science Collaboration 2023, The Open Journal of As-
   trophysics, 6, 17
Spergel D., et al., 2015, preprint, (arXiv:1503.03757)
Yamamoto M., et al., 2023, arXiv e-prints, p. arXiv:2303.08750
Zackay B., Ofek E. O., 2017, ApJ, 836, 187
```

APPENDIX A: S/N LOSS FROM COADDITION

Here we estimate the additional uncertainty in the measured flux when coadding, for the example of "matched-filter" photometry, where a linear fit is performed for the amplitude of a model. We consider an optimal estimator for a single unknown parameter that is linear in the observables. Let the model be $A\boldsymbol{m}$, where A is a scalar amplitude and \boldsymbol{m} is a normalized signal model, or template. Then the log-likelihood for A (assuming a Gaussian signal likelihood) and some data vector \boldsymbol{d} is

$$\log L = -\frac{1}{2} (\boldsymbol{d} - A\boldsymbol{m})^T C^{-1} (\boldsymbol{d} - A\boldsymbol{m}) - \frac{1}{2} \det((2\pi)^k C)$$
(A1)

where C is the noise covariance and k the size of m. The optimal estimator \hat{A} is the value that maximizes this expression for A. With some algebra, it can be shown that this value is:

$$\hat{A} = \frac{\boldsymbol{m}^T C^{-1} \boldsymbol{d}}{\boldsymbol{m}^T C^{-1} \boldsymbol{m}} \tag{A2}$$

and that the variance of \hat{A} is

$$var\hat{A} = \frac{1}{\boldsymbol{m}^T C^{-1} \boldsymbol{m}} \tag{A3}$$

In the case of photometry, m is the normalized profile of the star or galaxy, A is the measured flux, and d is the set of pixels on which the measurement will be made. The equations above are general, but for simplicity in what follows, we assume the noise comes from a uniform background, so there is no signal in the covariance. For a set of N images of the same sky, the data is the concatenation of the pixel values in each epoch, i.e., $d = \{d_1, d_2, ..., d_n\}$. This allows the template m to be the concatenation of the templates appropriate for each epoch, if for instance the PSF varies from exposure to exposure.

Now suppose we coadd the images using a straight mean, such that $\langle \boldsymbol{d} \rangle = \frac{1}{N} \sum_i d_i$, and the covariance matrix is $C_{\rm coadd} = \frac{1}{N^2} \sum_i C_i$. The template $\boldsymbol{m}_{\rm coadd}$ is then the mean

 $m_{\mathrm{coadd}} = \frac{1}{N} \sum_{i}^{i} m_{i}$ and the resulting operation is:

 $\hat{A}_{\text{coadd}} = \frac{\boldsymbol{m}_{\text{coadd}}^T \boldsymbol{C}_{\text{coadd}}^{-1} \langle \boldsymbol{d} \rangle}{\boldsymbol{m}_{\text{coadd}}^t \boldsymbol{C}_{\text{coadd}}^{-1} \boldsymbol{m}_{\text{coadd}}}$ (A4)

with estimator variance

12

$$\operatorname{var} \hat{A}_{\text{coadd}} = \frac{1}{\boldsymbol{m}_{\text{coadd}}^T C_{\text{coadd}}^{-1} \boldsymbol{m}_{\text{coadd}}},$$
 (A5)

where the indices in these expressions run over epochs. The multi-fitting method, by contrast, would use the optimal estimator for each epoch:

$$\hat{A}_{\text{multi}} = \frac{\sum_{i} \boldsymbol{m}_{i}^{T} C_{i}^{-1} \boldsymbol{d}_{i}}{\sum_{i} \boldsymbol{m}_{i}^{T} C_{i}^{-1} \boldsymbol{m}_{i}}$$
(A6)

with estimator variance

$$\operatorname{var} \hat{A}_{\text{multi}} = \frac{1}{\sum_{i} \boldsymbol{m}_{i}^{T} C_{i}^{-1} \boldsymbol{m}_{i}}.$$
(A7)

These variance estimators predict, for the case of background-only noise, that the variance of the coadd estimator is generally greater than or equal to that of the optimal estimator using the original images, assuming the templates are accurate. This is because the averaged signal will generally be less varied than the set of input images, such that $m^T C^{-1} m \sim \sum m^2$ is smaller for the coadd. In order to gain better intuition for this increased variance, we depart from generality in the data, and adopt a toy model for the signal. First, we assume that the noise in all images has the same statistical properties, with standard deviation η , such that the estimators become

$$\hat{A}_{\text{multi}} = \frac{\sum_{i} \boldsymbol{m}_{i}^{T} \boldsymbol{d}}{\sum_{i} \boldsymbol{m}_{i}^{T} \boldsymbol{m}_{i}}, \quad \text{var} \hat{A}_{\text{multi}} = \frac{\eta^{2}}{\sum_{i} \boldsymbol{m}_{i}^{T} \boldsymbol{m}_{i}}$$
(A8)

$$\hat{A}_{\text{coadd}} = \frac{\boldsymbol{m}_{\text{coadd}}^T \langle \boldsymbol{d} \rangle}{\boldsymbol{m}_{\text{coadd}}^T \boldsymbol{m}_{\text{coadd}}}, \quad \text{var} \hat{A}_{\text{coadd}} = \frac{\eta^2 / N}{\boldsymbol{m}_{\text{coadd}}^T \boldsymbol{m}_{\text{coadd}}}$$
 (A9)

We now assume that the template for the coadd is related to that in the original images by perturbations due to small variations in a scale of the object σ :

$$m_i = m_{\text{coadd}} + \Delta m_i$$
 (A10)

$$\approx m_{\text{coadd}} + \frac{\partial m_{\text{coadd}}}{\partial \sigma} \Delta \sigma$$
 (A11)

The ratio of variances then becomes

$$\frac{\operatorname{var} \hat{A}_{\operatorname{coadd}}}{\operatorname{var} \hat{A}_{\operatorname{multi}}} = 1 + \frac{1}{N} \frac{\sum_{i} \Delta \boldsymbol{m}_{i}^{T} \Delta \boldsymbol{m}_{i}}{\boldsymbol{m}_{\operatorname{coadd}}^{T} \boldsymbol{m}_{\operatorname{coadd}}}$$
(A12)

$$\approx 1 + \frac{(\Delta \sigma)^2}{N} \frac{\sum_{i} \left(\frac{\partial \boldsymbol{m}_{\text{coadd}}}{\partial \sigma}\right)_{i}^{T} \left(\frac{\partial \boldsymbol{m}_{\text{coadd}}}{\partial \sigma}\right)_{i}}{\boldsymbol{m}_{\text{coadd}}^{T} \boldsymbol{m}_{\text{coadd}}} \quad (A13)$$

We further assume the template is a round Gaussian

$$\boldsymbol{m}_{\text{coadd}} = \frac{1}{2\pi\sigma^2} e^{-r^2/2\sigma^2} \tag{A14}$$

with derivative

$$\frac{\partial \boldsymbol{m}_{\text{coadd}}}{\partial \sigma} = \frac{1}{2\pi\sigma^2} \frac{2}{\sigma} e^{r^2/2\sigma^2} \left(\frac{1}{2} \frac{r^2}{\sigma^2} - 1 \right). \tag{A15}$$

For these Gaussian models, all terms in equation (A12) can be readily calculated in the continuous limit, and we find

$$\left(\frac{\operatorname{var}\hat{A}_{\operatorname{coadd}}}{\operatorname{var}\hat{A}_{\operatorname{multi}}}\right)_{\operatorname{tov}} = 1 + 2\left(\frac{\Delta\sigma}{\sigma}\right)^{2} \tag{A16}$$

where $(\Delta \sigma)^2$ is to be interpreted as the rms variation of the size. We expect the increase in variance to be less for the case of large galaxies convolved by a PSF. If the galaxy is a round Gaussian with size σ_g and the PSF is a round Gaussian with size σ_p , and only the PSF size varies between images, we can use the chain rule to rewrite equation (A16) as

$$\left(\frac{\text{var}\hat{A}_{\text{coadd}}}{\text{var}\hat{A}_{\text{multi}}}\right)_{\text{toy}} = 1 + 2\left(\frac{\sigma_p^2}{\sigma_g^2 + \sigma_p^2}\right)^2 \left(\frac{\Delta\sigma_p}{\sigma_p}\right)^2 \tag{A17}$$

$$\equiv 1 + 2 \left(1 - R\right)^2 \left(\frac{\Delta \sigma_p}{\sigma_p}\right)^2 \tag{A18}$$

where we have used the definition of the resolution factor $R = \sigma_g^2/(\sigma_p^2 + \sigma_g^2)$. This confirms our intuition that measurements of large galaxies, with $R \sim 1$ will suffer less increase in variance. Note that, for this toy model, the template is not exactly equal to the mean of the individual templates. Thus we expect the toy model to slightly over-predict the increase in variance due to coaddition.